PCCP

PAPER

View Article Online
View Journal | View Issue

Cite this: *Phys. Chem. Chem. Phys.*, 2024, **26**, 24553

Separation of oxygen from nitrogen using a graphdiyne membrane: a quantum-mechanical study

Maryam A. Rafiei, *[ab] José Campos-Martínez, [a] Massimiliano Bartolomei, [a] Fernando Pirani, [c] Ali Maghari [b] and Marta I. Hernández *[a]

Efficient separation of oxygen and nitrogen from air is a process of great importance for many industrial and medical applications. Two-dimensional (2D) membranes are very promising materials for separation of gases, as they offer enhanced mass transport due to their smallest atomic thickness. In this work, we examine the capacity of graphdiyne (GDY), a new 2D carbon allotrope with regular subnanometric pores, for separating oxygen ($^{16}O_2$) from nitrogen ($^{14}N_2$). A quantum-mechanical model has been applied to the calculation of the transmission probabilities and permeances of these molecules through GDY using force fields based on accurate electronic structure computations. It is found that the $^{16}O_2/^{14}N_2$ selectivity (ratio of permeances) is quite high (*e.g.*, about 10^6 and 10^2 at 100 and 300 K, respectively), indicating that GDY can be useful for separation of these species, even at room temperature. This is mainly due to the N_2 transmission barrier ($\sim$0.37 eV) which is considerably higher than the O_2 one ($\sim$0.25 eV). It is also found that molecular motions are quite confined inside the GDY pores and that, as a consequence, quantum effects (zero-point energy) are significant in the studied processes. Finally, we explore the possibility of $^{18}O_2/^{16}O_2$ isotopologue separation due to these mass-dependent quantum effects, but it is found that the process is not practical since reasonable selectivities are concomitant with extremely small permeances.

Received 5th June 2024,
Accepted 30th August 2024

DOI: 10.1039/d4cp02287d

rsc.li/pccp

1 Introduction

Molecular oxygen (O_2) and nitrogen (N_2) are the major components of the atmosphere and, at the same time, are the two most demanded gases after hydrogen.[1–4] Nitrogen is used as a feedstock, as an inert atmosphere or as a cryogenic agent in many industrial and scientific applications. Oxygen is a key ingredient in industry (chemical, petrochemical, *etc.*) and an essential element in medical treatments. Extracting high purity oxygen from air is conventionally carried out using techniques such as cryogenic distillation and pressure swing adsorption; however, these techniques require large capital costs and high energy consumption. An interesting alternative is the utilization of separation membranes, and in fact there has been intense research on a large set of membranes for O_2/N_2 separation.[1,3–7] Besides good mechanical and chemical stability, an important requirement for membranes is a satisfactory trade-off between permeability (flow of the desired species) and selectivity (rejection of undesired species), as it is known that high selectivities are often accompanied by low permeances, and *vice versa*.[7,8] Since decreasing the thickness of the membrane increases the permeability, new two-dimensional (2D) materials are viewed as very promising candidates for achieving large transport fluxes together with acceptable selectivities.[9–13]

Among new 2D membranes, graphdiyne (GDY) stands out as an ideal material for gas separation applications. GDY is a planar carbon allotrope characterized by diacetylenic linkages joining graphene-like hexagons,[14] thus leading to an uniform web of triangular pores of subnanometric size. This membrane was first synthesized[15] in 2010 and, since then, there has been a burst of experimental and theoretical studies on its properties and applications,[16–21] including gas and isotopic separation.[22–25] The main separation mechanism in GDY is known as size sieving,[11,26] where molecules smaller than the pore size are able to permeate, while larger molecules are rejected, the sizes being correlated with kinetic diameters.[27] In this way, various studies have predicted high selectivities for the separation of H_2 and He from larger molecules.[28–31] It is

[a] *Instituto de Física Fundamental, Consejo Superior de Investigaciones Científicas (IFF-CSIC), Serrano 123, 28006 Madrid, Spain. E-mail: maryam.rafiei@ut.ac.ir, marta@iff.csic.es*
[b] *Department of Physical Chemistry, School of Chemistry, College of Science, University of Tehran, Tehran, Iran*
[c] *Departimento di Chimica, Biologia e Biotecnologie, Università di Perugia, via Elce di Sotto 8, Perugia, 06123, Italy*

worth pointing out that, due to the small size of the pores, the transport involves surmounting potential barriers, *i.e.*, the molecule–membrane interaction is repulsive at the pore center. Moreover, the molecular motion along directions transverse to the transmission path becomes confined and, as described by Beenakker *et al.*,[32] this feature can lead to an increase of the transmission barrier due to the zero-point energy (ZPE) associated to these transversal degrees of freedom, a quantum effect that is mass-dependent. Therefore, different isotopes would experience different effective barriers, allowing their separation (quantum sieving), as has been indeed found[33,34] for the separation by GDY of ^{4}He/^{3}He and D_2/H_2.

Separation processes of larger molecules by GDY have been also reported, for instance, CO_2/N_2[35] and CO_2/CH_4[36] separation, or the separation of O_2 from a mixture of harmful gases (Cl_2, HCl, *etc.*).[37] Selectivity can be enhanced by means of pore functionalization, as in the $CO_2/(N_2, CH_4)$ separation in oxygen-doped GDY[38] or NO/(O_2, CO) in boron-doped GDY.[39] As far as we are aware, there are no previous studies in which the transport properties of O_2 and N_2 through GDY are compared on an equal footing. This is the main goal of the present work.

In this paper, accurate electronic structure calculations are employed to obtain reliable estimations of the N_2–GDY and O_2–GDY interaction potentials. It is found that the transmission barriers are rather high (about 250 and 370 meV for O_2 and N_2, respectively) and that the interaction potential rapidly increases for molecular displacements perpendicular to the transmission path; in other words, the diatoms are confined at the pore center. Confinement associated to the rotational degrees of freedom also occurs. In this situation, significant quantum effects can appear despite the relatively large masses of these molecules.[32,40] Thus, a quantum approach has been here chosen to calculate transmission probabilities and permeances through GDY of the most abundant isotopologues of oxygen and nitrogen, $^{16}O_2$ and $^{14}N_2$, as well as their selectivity as a function of the temperature. In addition, we have also obtained the permeances of the very scarce $^{18}O_2$ isotopologue, with the aim to explore the extent of mass-dependent quantum effects and hence the possibility of $^{18}O_2/^{16}O_2$ separation, a process that is of great interest for several applications.[41]

The paper is organized as follows. The theoretical approach is presented is Section 2. In Section 3, results are reported and discussed with regard to interaction potential features, transmission probabilities, permeances, selectivities and the role of quantum effects. We end with some conclusions in Section 4.

2 Theoretical approach

We have investigated the transport of $^{14}N_2$, $^{16}O_2$ and $^{18}O_2$ through a periodic single GDY membrane. In this study, the molecules are considered as rigid rotors. Unlike H_2 molecules, heavier species like O_2 and N_2 are not expected to be well described as point-like particles (pseudoatoms) since the orientational anisotropy of the molecules is large.[40] Below we firstly present the electronic structure calculations and the force field used for the molecule–GDY interaction potential. Then, we describe the quantum mechanical model adopted for the calculation of the transmission probabilities, from which the permeances and selectivities can be obtained.

2.1 Interaction potential

Electronic structure calculations were performed to obtain interaction energies at the ''coupled'' supermolecular second-order Møller–Plesset perturbation (MP2C)[42] theory and density functional theory (DFT) levels by using Molpro[43] and ORCA 4.2.1[44] program packages, respectively. The (MP2C or DFT) interaction energies between a molecular prototype of GDY and the studied gases were obtained using

$$E_{\text{interaction}} = E_{\text{GDY+gas}} - (E_{\text{GDY}} + E_{\text{gas}}) \quad (1)$$

where $E_{\text{GDY+gas}}$, E_{GDY} and E_{gas} are the total energies of the adsorbed gas on GDY, isolated GDY and free gas, respectively. The resulting energies are obtained by applying the counterpoise correction[45] to the basis set superposition error and considering rigid bodies. Neither the ZPE of the monomers (the molecule and prototype are treated as rigid bodies) nor the ZPE corresponding to the molecule–GDY prototype interaction (to be taken into account afterwards in the dynamics calculations) are included in eqn (1). The GDY prototype used in the calculations is shown in the inset of Fig. 1(b). It correctly describes the features of the GDY triangular pore and its finite size has allowed us to carry out high level *ab initio* calculations, which are unavoidable to obtain benchmark estimations of the permeation barrier. The bond length values related to this geometry[46] are as follows: 1.431, 1.231, 1.395, 1.337 and 1.09 Å for the aromatic C–C, triple C–C, single C–C connecting aromatic and triple C–C bonds, single C–C between two triple C–C bonds and C–H bonds, respectively. In addition, internuclear distances for N_2 and O_2 are 1.1007 and 1.2080 Å, respectively.

Accurate MP2C calculations were performed to obtain benchmark electronic structure estimations of the interaction in the N_2–GDY system. In particular, distinct approach directions of the diatomic molecule as well as different (perpendicular and parallel) orientations of the latter with respect to the pore plane have been probed and the corresponding interaction energies were obtained by using the aug-cc-VQZ and aug-cc-VTZ basis sets[47] for N_2 and the GDY prototype, respectively. In addition, several DFT approaches were examined to assess their performances over the reference MP2C results. Among the DFT levels tested, the best results were obtained with the BP86[48] (a generalized gradient approximation (GGA) functional that depends on both the electron density and its gradient) and B3LYP[49] (a hybrid functional combining GGA and Hartree–Fock exchange) functionals. In these DFT calculations, a quadruple-zeta valence basis set with two sets of polarization functions (def2-QZVPP)[50] was used and the D3 dispersion correction[51] was applied. The primitive cut-off and integral threshold for the electron integral calculations were set to 2.5×10^{-12} and 2.5×10^{-11} E_h, respectively, and the tolerance energy for convergence between two self-consistent field cycles was set to 10^{-8} E_h. These choices provided the best agreement with the

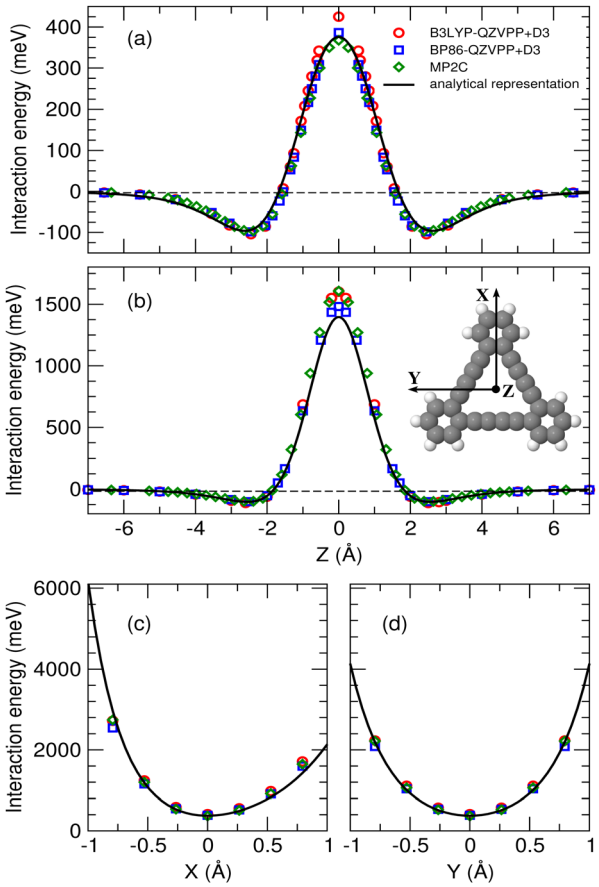

Fig. 1 Energy profiles for the interaction between N_2 and a GDY prototype, obtained from MP2C, B3LYP and BP86 calculations (points) as well as the ILJ representation (solid lines), (a) as functions of z for $(x,y) = (0,0)$, with the N_2 bond aligned perpendicularly to the prototype plane; (b) as in (a), with the N_2 molecular axis being parallel to the prototype plane and pointing to the triangle vertex; (c) as functions of x, for $(y,z) = (0,0)$, with the molecular axis perpendicular to the prototype plane (notice that the interaction is quite repulsive at $x \ll 0$ because the molecule becomes very close to the carbon atoms at the base of the triangular pore); (d) as functions of y, for $(x,z) = (0,0)$ and orientation as in (c). Inset of panel (b): Structure of the GDY prototype; the center of the coordinate system is at the center of the pore, and z and (x,y) axes are perpendicular and parallel to the prototype plane, respectively.

MP2C data. We have considered that these DFT levels, once validated for the N_2–GDY prototype, can be safely used to obtain reliable estimations of the O_2–GDY interaction, for which the MP2C approach is not suitable due to the O_2 open shell character.

Global interaction potentials for the interactions between O_2/N_2 and the GDY molecular prototype are analytically represented by the sum of pairwise contributions between the O or N atoms in the diatom and the carbon and hydrogen atoms of the prototype. The improved Lennard-Jones (ILJ)[52] formula is used to represent each of these atom–atom contributions, depending on R, the distance between O (or N) and the C or H atoms, and given by

$$V(r) = \varepsilon\left[\frac{6}{n(R)-6}\left(\frac{R_m}{R}\right)^{n(R)} - \frac{n(R)}{n(R)-6}\left(\frac{R_m}{R}\right)^{6}\right], \qquad (2)$$

where R_m and ε represent the equilibrium distance and well depth of the interacting pair, respectively. Moreover, $n(R) = \beta + 4.0(R/R_m)^2$, where β is a parameter defining the shape and stiffness of the potential. We have not added electrostatic contributions to this representation since, being the involved monomers neutral and apolar, they are expected to play quite a minor role. Owing to the similar effective atomic polarizabilities of O in O_2 and N in N_2, the ILJ potential parameters of O_2 and N_2 are expected to assume comparable values.[35] For simplicity, we use the same ILJ parameters for interactions with carbon atoms pertaining to different kinds of C–C bonds composing the GDY structure. This choice is supported by the fact that the atomic polarizabilities of those carbon atoms vary within a reduced range (from 1.05 to 1.3 Å^3).[53] Note that R_m, ε and β were not considered as fitting parameters since their zero-order values[35] have been varied within restricted ranges in order to maintain their proper physical meaning and transferability character. In particular, these parameters have been fine-tuned by exploiting the comparison with the reference MP2C, B3LYP-QZVPP+D3 and BP86-QZVPP+D3 interaction energies. The final optimized values are reported in Table 1.

In Fig. 1 and 2, we present the profiles of the interaction potentials between the GDY prototype and N_2 and O_2, respectively, obtained from the different levels of theory employed and the ILJ parametrization, for different approach directions and molecular orientations. From these figures, it can be concluded that there is a rather good agreement among the different levels of calculation considered as well as with the ILJ force field.

Finally, V, the interaction potential between O_2/N_2 and the extended GDY lattice (Fig. 3), is obtained by adding up all the pairwise ILJ contributions between the atoms of the molecule and the carbon atoms of the membrane for as many atoms in the lattice until a desired convergence in V is reached. The estimated errors in the determination of V are of about 0.02% for distances close to the membrane ($z < 4$ Å), increasing up to about 0.2% for larger distances ($z \approx 20$ Å).

Table 2 presents the molecule–GDY potential barriers as obtained for the different electronic structure methods and force field employed, corresponding to the centers of mass of the molecules placed at the center of the pore and perpendicularly oriented with respect to the GDY plane (for the GDY prototype, they correspond to the tops of the barriers depicted in Fig. 1 and 2). Notice that, within the ILJ representation, the barriers for the extended GDY are slightly lower than those corresponding to the GDY prototype. This is because the interaction with the extended layer involves a large number of

Table 1 ILJ optimized parameters for the atom–atom pairs involved in the interaction between O_2 or N_2 and the GDY molecular prototype. R_m and ε are in Å and in meV, respectively, while β is dimensionless

O_2/N_2–GDY	R_m	ε	β
O–C	3.741	4.001	6.5
N–C	3.801	4.140	6.5
O–H/N–H	3.490	2.076	8.0

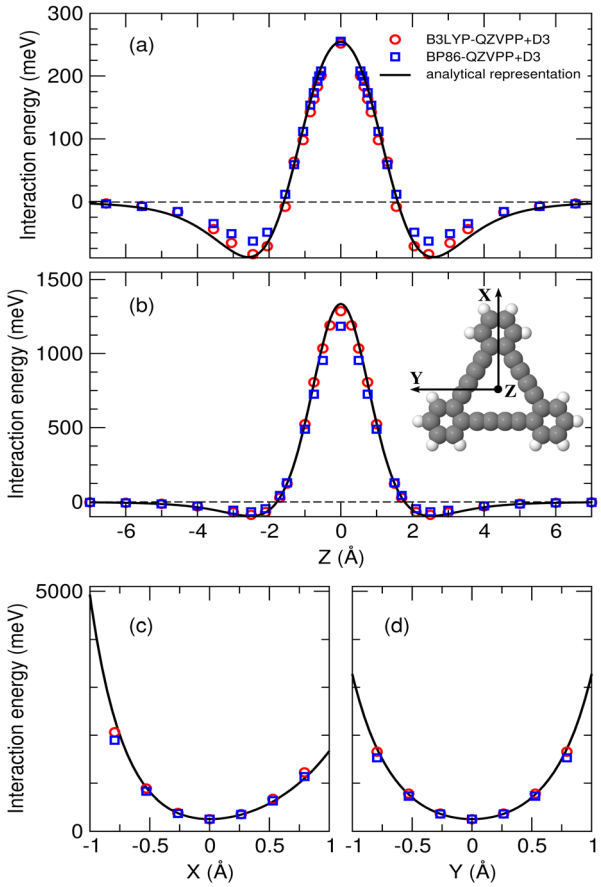

Fig. 2 Same as Fig. 1 for the O_2–GDY prototype energy interaction profiles obtained from B3LYP and BP86 calculations (points) as well as the ILJ analytical representation (solid lines).

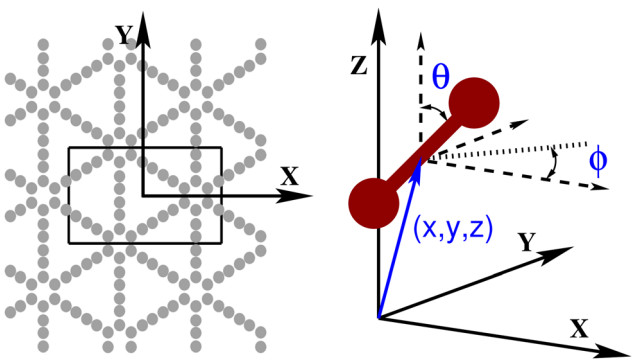

Fig. 3 Left panel: Scheme of the GDY membrane and coordinate frame: the (*X*,*Y*) plane is parallel to the membrane layer, *Z* is perpendicular to the membrane and the origin of the frame coincides with the center of one of the pores. The black rectangle depicts the unit cell. Right panel: Sketch of the coordinates used for the O_2/N_2–GDY systems. The position of the center of mass of the molecules is given by (*x*,*y*,*z*) and the molecular orientation by the polar and azimuthal angles θ and ϕ.

carbon atoms quite distant from the molecule but anyway contributing with a weak but attractive interaction.

Table 2 Potential barriers (in meV) for the transmission of N_2 and O_2 through either the GDY prototype or extended GDY, within the different approaches employed here. These barriers correspond to the energies for the molecules being at the center of the pores, with their axes oriented perpendicularly to GDY

		N_2	O_2
GDY prototype	MP2C	367.5	—
	B3LYP-QZVPP+D3	425.2	251.9
	BP86-QZVPP+D3	386.4	255.4
	ILJ	375.8	254.4
GDY	ILJ	368.4	247.3

Apart from the technical details reported here, the general features of the O_2–GDY and N_2–GDY interactions are discussed in detail in Section 3.

2.2 Quantum transmission probabilities, permeances and selectivities

The Hamiltonian for the interaction of a rigid diatomic molecule of mass m and bond length r_0 with a rigid membrane can be written as

$$H = \frac{-\hbar^2}{2m}\left[\frac{\partial^2}{\partial x^2}+\frac{\partial^2}{\partial y^2}+\frac{\partial^2}{\partial z^2}\right] + BJ^2 + V(\theta,\varphi,x,y,z), \qquad (3)$$

where $B = \hbar^2/(2mr_0^2)$ is the rotational constant, (x,y,z) is the position of the center of mass of the molecule and θ and ϕ are the polar and azimuthal angles defining the orientation of the molecular axis with respect to a laboratory frame (X,Y,Z), with (X,Y) being axes parallel to the membrane and Z a perpendicular axis passing through the center of a pore (see Fig. 3). The molecule–GDY interaction potential, V, obtained as described in the previous paragraph, is a function of these five coordinates. Finally, the first term in eqn (3) represents the kinetic energy of the molecular center of mass and J is the angular momentum operator divided by $\hbar$ such that

$$J^2 = -\frac{1}{\sin\theta}\frac{\partial}{\partial\theta}\sin\theta\frac{\partial}{\partial\theta} - \frac{1}{\sin^2\theta}\frac{\partial^2}{\partial\varphi^2}. \qquad (4)$$

Masses used in the calculations are 28.0134, 31.9898 and 35.9983 Da, while rotational constants are 0.2477, 0.1782 and 0.1585 meV for $^{14}N_2$, $^{16}O_2$ and $^{18}O_2$, respectively.

In this work, we apply an adiabatic separation between z, the coordinate representing the molecular incidence towards the membrane, and the remaining variables, (θ,ϕ,x,y), collectively denoted as Q. This approach is related to reaction path theories in molecular reactive scattering,[54,55] and treatments similar to the present one have been recently reported in simulations of the transmission of molecules through membranes.[34,56,57] In a first step, the Schrödinger equation for coordinates Q is solved for a set of fixed values of z, ranging from zero to the asymptotic region:

$$\left(\frac{-\hbar^2}{2m}\left[\frac{\partial^2}{\partial x^2}+\frac{\partial^2}{\partial y^2}\right] + BJ^2 + V(Q;z)\right)\Psi_n(Q;z) = W_n(z)\Psi_n(Q;z). \qquad (5)$$

The eigenvalues $W_n(z)$ become effective interaction potentials only depending on the molecule–membrane distance.

They are obtained from diagonalization of the associated Hamiltonian. Details on these calculations are given in the Appendix.

The lowest eigenvalue of eqn (5), $W_0(z)$, corresponds to the ZPE-corrected potential along the incidence direction. In this work, we will only consider this lowest effective potential, which is a reasonable approximation for the study of the transmission at low energies/temperatures, as discussed in more detail in the next section.

In a subsequent step, transmission probabilities as functions of the translational energy, $P(E)$, are computed by solving the scattering problem with a Hamiltonian only depending on the z coordinate:

$$H_z = \frac{-\hbar^2}{2m}\frac{\partial^2}{\partial z^2} + W_0(z). \quad (6)$$

This equation is solved by means of a time-dependent wavepacket approach, as carried out in related works.[31,34,58] An approach for solving the corresponding time-independent Schrödinger equation[59] was also employed for translational energies well below the potential barrier (deep tunneling regime). Details about these calculations are also provided in the Appendix.

As discussed in earlier works,[33,34] the probabilities $P(E)$ must be scaled by a factor γ that takes into account the fraction of the membrane area that is effective for the transmission

$$P^*(E) = \gamma P(E), \quad (7)$$

where $\gamma \approx n_p A_{eff}/A_{uc}$, with n_p being the number of pores per unit cell; A_{uc}, the unit cell area and A_{eff}, the effective size of the pore. The latter quantity is estimated from the area covered by the wavefunction at $z = 0$, specifically the area where $|\Psi_0(Q;0)|^2 > 10^{-4}$.

Permeances as functions of temperatures are then obtained from the transmission probabilities, expressed as functions of the velocity, $v_z = (2E/m)^{1/2}$, as[34]

$$S(T) = \frac{1}{K_B T}\int_0^\infty \mathrm{d}v_z f(v_z, T) v_z P^*(v_z), \quad (8)$$

with k_B being the Boltzmann constant and $f(v_z,T)$ the Maxwell–Boltzmann velocity distribution given by

$$f(v_z, T) = \left(\frac{m}{2\pi k_B T}\right)^{1/2} \exp\left(-\frac{1 m v_z^2}{2 k_B T}\right). \quad (9)$$

Finally, to compare the permeation efficiency of two species A and B, an A/B selectivity or separation factor is defined as

$$R_{A/B}(T) = \frac{S_A(T)}{S_B(T)}. \quad (10)$$

3 Results and discussion

We start this section with a discussion of the features of the N_2–GDY and O_2–GDY interaction potentials. Table 2 gives the energy barriers for the transmission of N_2 and O_2 through GDY (prototype and extended lattice) within different treatments. These barriers correspond to the saddle point in the transmission path of the molecules through the membrane, where the molecules are located at the center of the pore with their axes perpendicularly oriented with respect to the pore plane. The fact that the barrier for N_2 is higher than that for O_2 is an expected result since the N_2 kinetic diameter (3.64 Å) is larger than the O_2 one (3.46 Å).[27] These diameters are correlated with the widths of the ''electron clouds'' along the axes of the diatoms[27] or, similarly, with the perpendicular static dipole polarizabilities (10.24 and 8.23 a.u. for N_2 and O_2, respectively[60]). However, the large difference between the two barrier heights (the N_2 barrier is $\sim$50% higher than the O_2 one) could seem somewhat surprising, considering the relatively small difference in the molecular parameters. This feature can be understood from the repulsive character of the interactions around the pore region since, in this situation, slight variations in the molecular properties imply exponentially large differences in the resulting interaction energies.

Another characteristic of the molecule–GDY interactions is the large confinement of the molecules in the pore region. This feature can be easily noticed from the inspection of Fig. 1 and 2, which show scans of the interaction energies between the GDY prototype and N_2 and O_2, respectively, for various molecular orientations and approach directions. Firstly, panels (a) and (b) of these figures show the interaction energies for the diatoms approaching the pore center along the z direction, for perpendicular and parallel orientations, respectively. It can be seen that the barrier drastically increases for the parallel orientation of the molecules, *i.e.*, the rotational motion is hindered inside the GDY pore. On the other hand, panels (c) and (d) of the same figures depict the interaction potential for displacements around the pore center of the (perpendicularly oriented) molecules along the x and y directions, respectively. It is observed that the translational motion of the molecules is also affected by confinement.

Moving to the ZPE-corrected effective potentials, $W_0(z)$, obtained from solving eqn (5), they are shown using solid lines in Fig. 4 for $^{14}N_2$ and $^{16}O_2/^{18}O_2$, in the upper and lower panels, respectively. Dashed lines in these plots correspond to optimized molecule–GDY potentials, $V_m(z)$, which are obtained by selecting the values of (θ,ϕ,x,y) minimizing $V(\theta,\phi,x,y;z)$ at each z, *i.e.*, $V_m(z) = (\theta_m,\phi_m,x_m,y_m;z)$. The extent of ZPE in these systems can be estimated by the difference between $W_0(z)$ and $V_m(z)$. It can be noticed that the ZPE is quite significant near the membrane pore: at $z = 0$, its contribution to the barrier height of W_0 amounts to about 12–15%. This is due to the confinement of the molecules in this region, discussed in the previous paragraph. Neglecting the ZPE contribution can lead to a considerable overestimation of the permeances. Indeed, if this quantum effect were neglected, it is estimated that $^{16}O_2$ and $^{14}N_2$ permeances would be about four orders of magnitude larger at a temperature of 50 K, the factor being reduced to one order of magnitude at 200 K. Concerning the oxygen isotopologues (inset in the lower panel of Fig. 4), it is noted that there

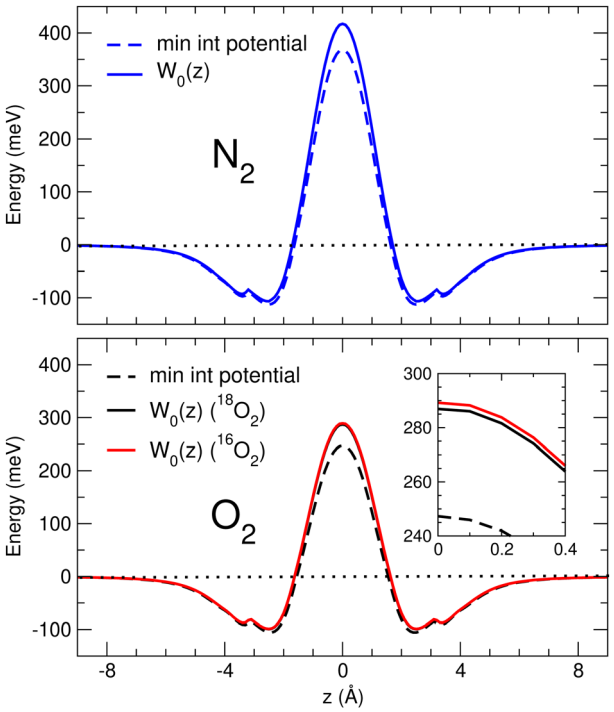

Fig. 4 Upper panel: Optimized (dashed lines) and ZPE-corrected (solid lines) potentials (in meV) for the $^{14}N_2$–GDY as functions of z (in Å). Lower panel: Same for $^{16}O_2$–GDY and $^{18}O_2$–GDY. An enlarged image of these potentials near the top of the barriers is shown in the inset. See text for details.

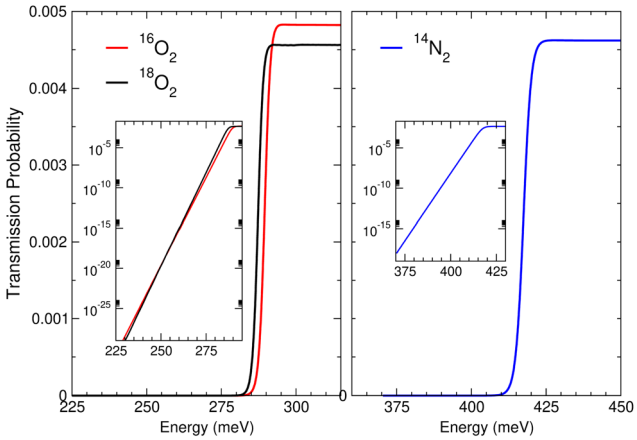

Fig. 5 Left panel: Transmission probabilities as functions of the translational energy for $^{16}O_2$ (red) and $^{18}O_2$ (black) through GDY. The behavior of these probabilities (in a logarithmic scale) for energies below the effective potential barrier (tunneling region) is given in the inset. Right panel: Same for the transmission probability of $^{14}N_2$ through GDY. See text for discussion.

is a small but clear difference between their ZPE-corrected potential barriers (286.9 and 289.2 meV for $^{18}O_2$ and $^{16}O_2$, respectively). The effect of this difference on the permeances is discussed below.

Regarding the behavior of the ZPE at larger distances to the GDY layer, it is observed from Fig. 4 that the ZPE monotonously decreases with z and that at the minimum of both W_0 and V_m potentials, at $z \approx 2.5$ Å, it becomes almost negligible. It can be also noticed that both $V_m(z)$ and $W_0(z)$ reach a further (local) minimum at $z \approx 3.5$ Å. This feature is due to the topography of the O_2–membrane and N_2–membrane interaction potentials: the absolute minima at $z \approx 2.5$ Å correspond to the molecules placed on top of the triangular-like pores, while, in the secondary minima, they sit on top of the hexagonal pores of GDY (Fig. 3), at a larger z distance.

The transmission probabilities of $^{16}O_2$, $^{18}O_2$ and $^{14}N_2$ through GDY are reported in Fig. 5. It can be seen that these probabilities rise up at translational energies close to the barriers of the corresponding ZPE-corrected potentials (Fig. 4). In particular, it is seen that the $^{16}O_2$ probability emerges at slightly larger energies than the $^{18}O_2$ one, in correspondence with its higher ZPE (inset of Fig. 4). After their thresholds, the probabilities reach nearly similar plateaus (0.0046–0.0048) which are associated to γ, the effective size of the pore for each species. Comparing the two oxygen isotopologues, the effective pore size for $^{16}O_2$ is larger than that of $^{18}O_2$ because, being $W_0(z = 0)$ higher for the lighter molecule, the corresponding wavefunction extends over a larger region of the coordinate space. The behavior of the probabilities at energies lower than the effective barriers is shown in the insets of Fig. 5, where it can be seen that, in this tunneling regime, the probabilities decrease exponentially as the energy decreases. It can be noticed that the $^{16}O_2$ probabilities decrease less rapidly than the $^{18}O_2$ ones and eventually, for energies below ~252 meV (close to the barrier of the "bare" O_2–GDY potential), the $^{16}O_2$ probabilities become larger than the $^{18}O_2$ ones. This behavior is due to the tunneling effect, which is more favourable for the lighter species. In conclusion, these moderately heavy molecules exhibit sizable quantum effects (ZPE, tunneling) in their passage through GDY. It is worth mentioning that this behavior of the probabilities is very similar to that found for lighter species (He[33,58,61] and H_2[34]) and their isotopologues.

The permeances of GDY for the transport of nitrogen and oxygen isotopologues are reported in the upper panel of Fig. 6 for temperatures between 20 and 300 K. In this temperature range, the $^{14}N_2$ ($^{16}O_2$) de Broglie wavelength approximately varies from 0.28(0.26) Å, at 300 K, to 1.07(1.00) Å, at 20 K. It can be seen that all permeances are extremely small at the lowest temperatures; however, they rapidly raise with temperature up to about 100 K, where there is a more moderate increasing rate. This is the typical behavior of activated processes. Due to the fact that the transmission barrier of $^{16}O_2$ is considerably lower than that of $^{14}N_2$, the $^{16}O_2$ permeation is much larger and, consequently, the $^{16}O_2/^{14}N_2$ selectivity is very large, especially at low temperatures, as can be observed in the lower panel of Fig. 6.

At this point, it is worth recalling that the permeances of Fig. 6 correspond to the use of the lowest eigenvalue of eqn (5), $W_0(z)$, as the effective interaction potential. The subsequent effective potentials, $W_{n>0}(z)$, should also contribute to the total transmission probabilities/permeances, but, since they involve

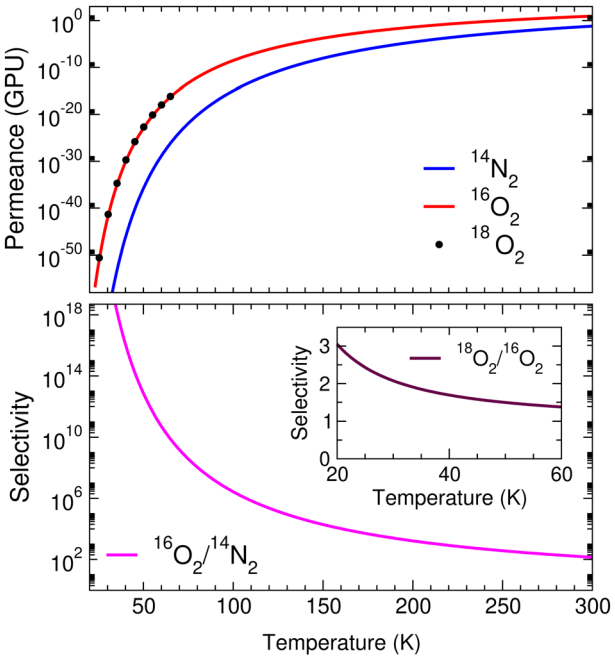

Fig. 6 Upper panel: Permeances (log scale) of GDY for the transport of $^{14}N_2$, $^{16}O_2$ and $^{18}O_2$ in the temperature range 20–300 K (1 GPU = 3.35 × 10^{-10} mol m^{-2} s^{-1} Pa^{-1}). Lower panel: Selectivity (log scale) for $^{16}O_2/^{14}N_2$ in the same temperature range. Inset: Selectivity for the separation of oxygen isotopologues $^{18}O_2/^{16}O_2$ in the 20–60 K range. See text for discussion.

somewhat higher transmission barriers, these contributions are unimportant at low energies/temperatures. Fig. 7 presents a diagram of the lowest eigenvalues of eqn (5) at $z = 0$ for $^{16}O_2$ and $^{14}N_2$ (transmission barriers of $W_n(z)$, n = 0–20). We have estimated that the $^{16}O_2$ and $^{14}N_2$ permeances corresponding to the excited effective potentials $W_{n>0}(z)$ are negligible below 100 K (less than 10% of the permeances from $W_0(z)$ in this temperature range). In other words, the permeances reported in Fig. 6 are accurate enough up to 100 K. Above this temperature, they are lower bounds of the total permeances because the contributions from the higher effective potentials are to be added. Nevertheless, we expect that the O_2/N_2 selectivity would keep similar values to those shown in Fig. 6. The reason for this assertion can be better understood looking at Fig. 7, where it can be seen that the density of energy levels in the O_2 spectrum is pretty similar to that in the N_2 spectrum. As a consequence, the contribution of the $W_{n>0}$ potentials to the total permeance should be of the same order of magnitude for both molecules, hence approximately preserving the selectivity. Finally, it is worth noting that the O_2 permeance obtained at 300 K, of about 10 GPU, is close (considering that it is a lower bound, as discussed above) to the minimum accepted value of 20 GPU for industrial applications.[62] At this temperature, the O_2/N_2 selectivity is ∼100, a value well above 6, the minimum acceptable value for separation applications.[62] To put this result into context, O_2/N_2 selectivities in the range of 3–15 have been obtained using a variety of polymer-, perovskite- and carbon-based membranes.[1] For thin films of graphene, in particular, a selectivity of 6 has been reported for five layers of graphene

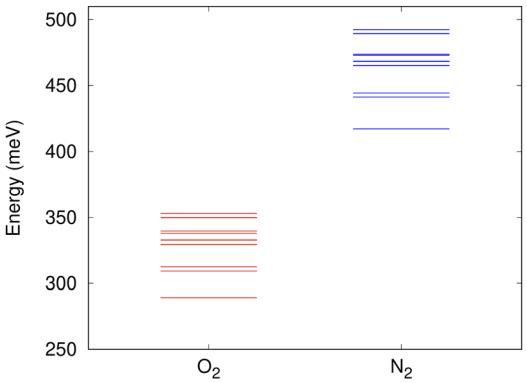

Fig. 7 Lowest eigenvalues of eqn (5), W_n (n = 0–20) at $z = 0$ for $^{16}O_2$ and N_2. See text for discussion.

synthesized by chemical vapor deposition, supported on a permeable polymer.[63] On the side of the theoretical simulations, we mention a molecular dynamics study of the O_2/N_2 separation using a bilayer nanoporous graphene where a selectivity factor of 26 and a permeance of 5 × 10^5 GPU were found for an optimum pore size of 3.45 Å.[2] In summary, it is found that GDY could be an useful membrane for the separation of oxygen from air, even under room temperature conditions, a result that would be worth checking experimentally. Also, it would be important to investigate the effect of the interactions among the molecules and the initial O_2/N_2 concentration on the selectivity, a study that could be carried out by means of molecular dynamics simulations.

The permeances of the heavier oxygen isotopologue $^{18}O_2$ are also shown in the upper panel of Fig. 6 (points). In the graph, it appears to be indistinguishable from the $^{16}O_2$ permeance, as in fact both $^{18}O_2$ and $^{16}O_2$ permeances have very close values. Their difference can be better noticed by means of their ratio, *i.e.*, the $^{18}O_2/^{16}O_2$ selectivity, which is shown in the inset of the lower panel of Fig. 6. It is found that the selectivity is very small (∼1.5) for temperatures of 50 K and higher; however, it steadily increases as the temperature decreases, reaching a value of 3 at 20 K. This trend favouring the transport of the heavier molecule is due to the lower value of its ZPE-corrected potential barrier. Extending the calculation of the permeances to lower temperatures, it is found that the $^{18}O_2/^{16}O_2$ selectivity reaches a maximum value of 4.5 at about 13.5 K, then rapidly decreases for lower temperatures. This behavior – also found for the transport of $^4He/^3He$ and D_2/H_2 through GDY[33,34] – is due to the onset of tunneling which favors the transmission of the lighter species at sufficiently low temperatures. At any rate, the present results indicate that transmission through GDY is not a practical method for separating $^{18}O_2$ from $^{16}O_2$, primarily because the permeances are negligibly small at the temperatures of eventual interest.

4 Conclusion

Transport of oxygen and nitrogen molecules through GDY has been studied by means of quantum mechanical methods, with

the primary aim of assessing the capability of this membrane to efficiently separate these two main components of air. Density functional theory calculations, benchmarked against accurate *ab initio* methods, have been applied to determine the interaction potential between O_2 (and N_2) and a molecular prototype of GDY and these data have served to build reliable analytical representations of these potentials, based on an improved Lennard-Jones formulation. It has been found that the barrier for transmission through GDY is higher for N_2 than for O_2, the result being rationalized from the sensitivity in the repulsive regime of the interaction potential to the molecular properties. Transmission probabilities and permeances were obtained from time-dependent wave-packet simulations using effective interaction potentials that include quantum corrections (ZPE). These quantum effects make a significant contribution to the height of the effective potential barriers due to the confinement of the molecular motions in the pore region. As a consequence of their different transmission barriers, the permeances for $^{16}O_2$ transport are much larger than those for $^{14}N_2$ over a large range of temperatures (20–300 K), predicting in this way that GDY is a very promising material for the separation and purification of oxygen from air. However, separation of the scarce $^{18}O_2$ isotopologue from the abundant $^{16}O_2$ one was found to be unfeasible.

Given the good prospects for the oxygen–nitrogen separation by GDY, it would certainly be worth experimentally checking the present predictions. Recently, Zhou *et al.*[25] have pioneered experiments on the permeation of gases of small molecules through multilayer GDY, so their set-up might be ideal to study a mixture of oxygen and nitrogen. In addition, it would be interesting to complement this study with other theoretical investigations, in particular molecular dynamics simulations,[2,64] which would provide insights into the role of aspects not considered here, such as the molecule–molecule (self or mixed) interactions, the adsorption on the membrane, or membrane vibrations, into the O_2/N_2 transport dynamics.

Data availability

The data that support the findings of this study are available from the corresponding authors upon reasonable request.

Conflicts of interest

There are no conflicts to declare.

Appendix: calculations of effective potentials and transmission probabilities

The ZPE-corrected interaction potentials, $W_0(z)$, are obtained from diagonalization of the Hamiltonian of eqn (5), represented using the basis set

$$\Phi_{lm,i,j}(Q) = \mathscr{Y}_{lm}(\theta,\phi)\psi_i(x)\psi_j(y), \tag{11}$$

where $\mathscr{Y}_{lm}$ are tesseral (real) spherical harmonics[65] and $\psi_i(x)$ and $\psi_j(y)$ are discrete variable representation (DVR) functions.[66] It should be noted that the shape of the interaction potential, $V(\theta,\phi,x,y;z)$, changes considerably as z increases from zero up to the asymptotic region. It is then necessary to adjust the properties of the basis set for the different molecule–membrane distances, in order to make the calculations affordable. Thus, for $z = 0$, where V quickly becomes very repulsive for (x,y) values away from the center of the pore (panels (c) and (d) of Fig. 1 and 2), we used a set of $N = 15$ "fixed-node" DVR basis functions:[66]

$$\psi_i(x) = \frac{2}{\sqrt{(N+1)a_x}}\sum_{n=1}^{N}\sin\left[n\pi\left(\frac{x+a_x/2}{a_x}\right)\right]\sin\left[\frac{ni\pi}{N+1}\right], \tag{12}$$

defined in $[-a_x/2,a_x/2]$, the size of this box being very small, a_x = 0.6 Å (analogously for the y coordinate). The potential is also very anisotropic at $z = 0$ (panels (a) and (b) of Fig. 1 and 2) so a large number of spherical harmonics (up to $l_{max} = 18$) were needed to attain convergence. As z increases, the concavity and anisotropy of the potential decrease, and therefore the box sizes (a_x,a_y) are increased and the size of the angular basis set can be gradually reduced (to about $l_{max} = 6$). For $z \approx 3$, the eigenfunctions turn out to be very extended, covering almost all the unit cell, and for $z > 3$ Å it becomes necessary to work with a basis function satisfying periodic boundary conditions, such as the periodic DVR basis set[66]

$$\psi_i(x) = \frac{1}{\sqrt{a_x N}}\sum_{n=1}^{N}\cos[k_n(x-x_i)], \tag{13}$$

where $k_n = (2n - N - 1)\pi/a_x$ and $x_i = (2i - N - 1)a_x/2N$ (analogously for y). In the calculations, we have used a set of $N = 37$ and 21 functions for the x and y coordinates, respectively, extended over the unit cell size.

The next step in our procedure concerns solving the quantum problem for the Hamiltonian H_z of eqn (6) to obtain the transmission probabilities. As in previous works,[31,58] we apply the time-dependent wave packet method using the initial wave packet[67]

$$\Psi(z,t=0) = \left(\frac{2\mathrm{Im}(\alpha)}{\pi\hbar}\right)^{1/4}\exp\left[i\alpha(z-z_0)^2/\hbar + ik_{z0}(z-z_0)\right], \tag{14}$$

where α is a pure imaginary number ($0.28i$ a.u.) related to the width of $|\Psi|^2$, z_0 is the wave packet central position (sufficiently distant from the membrane, z_0 = 35 Å), and k_{z0} is the central wave vector (such that the central translational energy is $E_0 = \hbar^2 k_{z_0}{}^2/2m$). Calculations are run for various k_{z_0} values to adequately represent the transmission probabilities in the desired energy range. The wave packet is represented in a grid (8192 points in the range of $z = -50$ to 50 Å) and is propagated in time using the evolution operator $\exp(-iH_z t/\hbar)$ and employing the split-operator method[68] where, at each time step (0.02 fs), this operator is approximately split as a product of potential and kinetic evolution operators, which are successively applied to

the wave packet. Propagation with the potential and kinetic terms is performed in the space and momentum representations, respectively, and the fast Fourier transform is used to transform the wave packet between both representations. Finally, the transmission probability is obtained from the flux of the stationary wave function at a point z_f (−5 Å) separating transmitted waves from incident and reflected ones[31,69]; in turn, the stationary wave function is obtained from a Fourier transform of the time-dependent wave packet. In the deep tunneling regime, we have also applied the method proposed by Cedillo,[59] in which a Numerov recursion is employed to solve the associated time-independent Schrödinger equation, with a step size of 0.016 Å and integrating between −50 and 50 Å.

Acknowledgements

Maryam A. Rafiei thanks the International and Research Councils of the University of Tehran for giving her the opportunity to spend a research trip at the Instituto de Fsica Fundamental (IFF-CSIC). We also thank Prof. M. Mella for useful discussions. The work has been funded through Spanish AEI grants PID2020-114957GB-I00/AEI/10.13039/501100011033 and PID2020-114654GB-I00/AEI/10.13039/501100011033. Allocation of computing time by CESGA (Spain) is also acknowledged.

Notes and references

1 N. F. Himma, A. K. Wardani, N. Prasetya, P. T. Aryanti and I. G. Wenten, Recent progress and challenges in membrane-based O_2/N_2 separation, *Rev. Chem. Eng.*, 2019, **35**, 591–625.
2 S. Wang, S. Dai and D.-E. Jiang, Entropic selectivity in air separation via a bilayer nanoporous graphene membrane, *Phys. Chem. Chem. Phys.*, 2019, **21**, 16310–16315.
3 B. Adhikari, C. J. Orme, J. R. Klaehn and F. F. Stewart, Technoeconomic analysis of oxygen-nitrogen separation for oxygen enrichment using membranes, *Sep. Purif. Technol.*, 2021, **268**, 118703.
4 D. González-Revuelta, M. Fallanza, A. Ortiz and D. Gorri, Thin-film composite matrimid-based hollow fiber membranes for oxygen/nitrogen separation by gas permeation, *Membranes*, 2023, **13**, 218.
5 K. Chong, S. Lai, H. Thiam, H. Teoh and S. Heng, Recent progress of oxygen/nitrogen separation using membrane technology, *J. Eng. Sci. Technol.*, 2016, **11**, 1016–1030.
6 S. S. Karim, S. Farrukh, A. Hussain, T. Noor and M. Younas, A comprehensive overview of dual-layer composite membrane for air (O_2/N_2) separation, *Polym. Polym. Compos.*, 2021, **29**, S1630–S1640.
7 Y. Liu, X. Chen, T. Han, C. Wang, H. Liu, Y. Sun, P. Zheng, H. Zhang and S. Luo, Rational macromolecular design and strategies to tune the microporosity for high-performance O_2/N_2 separation membranes, *Sep. Purif. Technol.*, 2024, **334**, 125978.
8 L. M. Robeson, The upper bound revisited, *J. Membr. Sci.*, 2008, **320**, 390–400.
9 S. P. Koenig, L. Wang, J. Pellegrino and J. S. Bunch, Selective molecular sieving through porous graphene, *Nat. Nanotechnol.*, 2012, **7**, 728–732.
10 L. Huang, M. Zhang, C. Li and G. Shi, Graphene-based membranes for molecular separation, *J. Phys. Chem. Lett.*, 2015, **6**, 2806–2815.
11 L. Wang, M. S. Boutilier, P. R. Kidambi, D. Jang, N. G. Hadjiconstantinou and R. Karnik, Fundamental transport mechanisms, fabrication and potential applications of nanoporous atomically thin membranes, *Nat. Nanotechnol.*, 2017, **12**, 509–522.
12 L. F. Villalobos, D. J. Babu, K.-J. Hsu, C. Van Goethem and K. V. Agrawal, Gas separation membranes with atom-thick nanopores: The potential of nanoporous single-layer graphene, *Acc. Mater. Res.*, 2022, **3**, 1073–1087.
13 M.-C. Ferrari, Recent developments in 2D materials for gas separation membranes, *Curr. Opin. Chem. Eng.*, 2023, **40**, 100905.
14 R. Baughman, H. Eckhardt and M. Kertesz, Structure-property predictions for new planar forms of carbon: Layered phases containing sp^2 and sp atoms, *J. Chem. Phys.*, 1987, **87**, 6687–6699.
15 G. Li, Y. Li, H. Liu, Y. Guo, Y. Li and D. Zhu, Architecture of graphdiyne nanoscale films, *Chem. Commun.*, 2010, **46**, 3256–3258.
16 J. Zhou, X. Gao, R. Liu, Z. Xie, J. Yang, S. Zhang, G. Zhang, H. Liu, Y. Li, J. Zhang and Z. Liu, Synthesis of graphdiyne nanowalls using acetylenic coupling reaction, *J. Am. Chem. Soc.*, 2015, **137**, 7596–7599.
17 C. Huang, Y. Li, N. Wang, Y. Xue, Z. Zuo, H. Liu and Y. Li, Progress in research into 2D graphdiyne-based materials, *Chem. Rev.*, 2018, **118**, 7744–7803.
18 C. Owais, A. James, C. John, R. Dhali and R. S. Swathi, Selective permeation through one-atom-thick nanoporous carbon membranes: theory reveals excellent design strategies, *J. Phys. Chem. B*, 2018, **122**, 5127–5146.
19 R. Sakamoto, N. Fukui, H. Maeda, R. Matsuoka, R. Toyoda and H. Nishihara, The accelerating world of graphdiynes, *Adv. Mater.*, 2019, **31**, 1804211.
20 X. Gao, H. Liu, D. Wang and J. Zhang, Graphdiyne: synthesis, properties, and applications, *Chem. Soc. Rev.*, 2019, **48**, 908–936.
21 X. Yang, Z. Qu, S. Li, M. Peng, C. Li, R. Hua, H. Fan, J. Caro and H. Meng, Ultra-fast preparation of large-area graphdiyne-based membranes via alkynylated surface-modification for nanofiltration, *Angew. Chem.*, 2023, **62**, e202217378.
22 H. Qiu, M. Xue, C. Shen, Z. Zhang and W. Guo, Graphynes for water desalination and gas separation, *Adv. Mater.*, 2019, **31**, 1803772.
23 M. Bartolomei, E. Carmona-Novillo, M. I. Hernández, J. Campos-Martínez, F. Pirani, G. Giorgi and K. Yamashita, Penetration barrier of water through graphynes' pores: first-principles predictions and force field optimization, *J. Phys. Chem. Lett.*, 2014, **5**, 751–755.
24 J. Xu and S. Meng, Molecular transport across a two-dimensional nanomesh membrane–graphdiyne, *J. Phys. D: Appl. Phys.*, 2020, **53**, 493003.

25 Z. Zhou, Y. Tan, Q. Yang, A. Bera, Z. Xiong, M. Yagmurcukardes, M. Kim, Y. Zou, G. Wang, A. Mishchenko, I. Timokhin, C. Wang, H. Wang, C. Yang, Y. Lu, R. Boya, H. Liao, S. Haigh, H. Liu, F. M. Peeters, Y. Li, A. K. Geim and S. Hu, Gas permeation through graphdiyne-based nanoporous membranes, *Nat. Commun.*, 2022, **13**, 4031.

26 Y. Jiao, A. Du, M. Hankel and S. C. Smith, Modelling carbon membranes for gas and isotope separation, *Phys. Chem. Chem. Phys.*, 2013, **15**, 4832–4843.

27 N. Mehio, S. Dai and D.-E. Jiang, Quantum mechanical basis for kinetic diameters of small gaseous molecules, *J. Phys. Chem. A*, 2014, **118**, 1150–1154.

28 Y. Jiao, A. Du, M. Hankel, Z. Zhu, V. Rudolph and S. C. Smith, Graphdiyne: a versatile nanomaterial for electronics and hydrogen purification, *Chem. Commun.*, 2011, **47**, 11843–11845.

29 S. W. Cranford and M. J. Buehler, Selective hydrogen purification through graphdiyne under ambient temperature and pressure, *Nanoscale*, 2012, **4**, 4587–4593.

30 H. Zhang, X. He, M. Zhao, M. Zhang, L. Zhao, X. Feng and Y. Luo, Tunable hydrogen separation in sp-sp^2 hybridized carbon membranes: A first-principles prediction, *J. Phys. Chem. C*, 2012, **116**, 16634–16638.

31 M. Bartolomei, E. Carmona-Novillo, M. I. Hernández, J. Campos-Martínez, F. Pirani and G. Giorgi, Graphdiyne pores: ''ad hoc'' openings for helium separation applications, *J. Phys. Chem. C*, 2014, **118**, 29966–29972.

32 J. J. M. Beenakker, V. D. Borman and S. Y. Krylov, Molecular transport in subnanometer pores: zero-point energy, reduced dimensionality and quantum sieving, *Chem. Phys. Lett.*, 1995, **232**, 379–382.

33 A. Gijón, J. Campos-Martínez and M. I. Hernández, Wave packet calculations of the quantum transport of atoms through nanoporous membranes, *J. Phys. Chem. C*, 2017, **121**, 19751–19757.

34 E. García-Arroyo, J. Campos-Martínez, M. Bartolomei, F. Pirani and M. I. Hernández, Molecular hydrogen isotope separation by a graphdiyne membrane: a quantum-mechanical study, *Phys. Chem. Chem. Phys.*, 2022, **24**, 15840–15850.

35 Y. B. Apriliyanto, N. Faginas Lago, A. Lombardi, S. Evangelisti, M. Bartolomei, T. Leininger and F. Pirani, Nanostructure selectivity for molecular adsorption and separation: the case of graphyne layers, *J. Phys. Chem. C*, 2018, **122**, 16195–16208.

36 S. Mahnaee, M. J. López and J. A. Alonso, Separation of CO_2/CH_4 gas mixtures using nanoporous graphdiyne and boron-graphdiyne membranes: influence of the pore size, *Phys. Chem. Chem. Phys.*, 2024, **26**, 15916–15926.

37 Z. Meng, X. Zhang, Y. Zhang, H. Gao, Y. Wang, Q. Shi, D. Rao, Y. Liu, K. Deng and R. Lu, Graphdiyne as a high-efficiency membrane for separating oxygen from harmful gases: a first-principles study, *ACS Appl. Mater. Interfaces*, 2016, **8**, 28166–28170.

38 L. Zhao, P. Sang, S. Guo, X. Liu, J. Li, H. Zhu and W. Guo, Promising monolayer membranes for CO_2/N_2/CH_4 separation: Graphdiynes modified respectively with hydrogen, fluorine, and oxygen atoms, *Appl. Surf. Sci.*, 2017, **405**, 455–464.

39 M. A. Rafiei and A. Maghari, Theoretical study of NO/CO/O_2 gas separation using graphdiyne and boron-doped graphdiyne membranes - A new corresponding state principle, *Comput. Theor. Chem.*, 2024, **1235**, 114534.

40 G. Garberoglio, Quantum states of rigid linear rotors confined in a slit pore: quantum sieving of hydrogen isotopes and extreme one dimensional confinement, *Eur. Phys. J. D*, 2009, **51**, 185–191.

41 S. K. Ujjain, A. Bagusetty, Y. Matsuda, H. Tanaka, P. Ahuja, C. de Tomas, M. Sakai, F. Vallejos-Burgos, R. Futamura, I. Suarez-Martinez, M. Matsukata, A. Kodama, G. Garberoglio, Y. Gogotsi, J. Karl Johnson and K. Kaneko, Adsorption separation of heavier isotope gases in subnanometer carbon pores, *Nat. Commun.*, 2021, **12**, 2041.

42 M. Pitonak and A. Heßelmann, Accurate intermolecular interaction energies from a combination of MP2 and TDDFT response theory, *J. Chem. Theory Comput.*, 2010, **6**, 168–178.

43 H. J. Werner, P. J. Knowles, R. Lindh, F. R. Manby, M. Schütz and some others, *MOLPRO, Version 2022.2, a Package of Ab Initio Programs*, 2022, see **https://www.molpro.net/**.

44 F. Neese, The ORCA program system, *Wiley Interdiscip. Rev.: Comput. Mol. Sci.*, 2012, **2**, 73–78.

45 S. F. Boys and F. Bernardi, The calculation of small molecular interactions by the differences of separate total energies. Some procedures with reduced errors, *Mol. Phys.*, 1970, **19**, 553–566.

46 Y. Pei, Mechanical properties of graphdiyne sheet, *Phys. B*, 2012, **407**, 4436–4439.

47 R. A. Kendall, J. Dunning, H. Thom and R. J. Harrison, Electron affinities of the first-row atoms revisited. Systematic basis sets and wave functions, *J. Chem. Phys.*, 1992, **96**, 6796–6806.

48 A. D. Becke, Density-functional exchange-energy approximation with correct asymptotic behavior, *Phys. Rev. A*, 1988, **38**, 3098.

49 C. Lee, W. Yang and R. G. Parr, Development of the Colle-Salvetti correlation-energy formula into a functional of the electron density, *Phys. Rev. B: Condens. Matter Mater. Phys.*, 1988, **37**, 785.

50 F. Weigend and R. Ahlrichs, Balanced basis sets of split valence, triple zeta valence and quadruple zeta valence quality for H to Rn: Design and assessment of accuracy, *Phys. Chem. Chem. Phys.*, 2005, **7**, 3297–3305.

51 S. Grimme, J. Antony, S. Ehrlich and H. H. Krieg, A consistent and accurate ab initio parametrization of density functional dispersion correction (DFT-D) for the 94 elements H-Pu, *J. Chem. Phys.*, 2010, **132**, 154104.

52 F. Pirani, S. Brizi, L. Roncaratti, P. Casavecchia, D. Cappelletti and F. Vecchiocattivi, Beyond the Lennard-Jones model: A simple and accurate potential function probed by high resolution scattering data useful for molecular dynamics simulations, *Phys. Chem. Chem. Phys.*, 2008, **10**, 5489–5503.

53 A. Gavezzotti, Calculation of intermolecular interaction energies by direct numerical integration over electron densities. 2. An improved polarization model and the evaluation of dispersion and repulsion energies, *J. Phys. Chem. B*, 2003, **107**, 2344–2353.
54 W. H. Miller, N. C. Handy and J. E. Adams, Reaction path Hamiltonian for polyatomic molecules, *J. Chem. Phys.*, 1980, **72**, 99–112.
55 J. L. Bao and D. G. Truhlar, Variational transition state theory: theoretical framework and recent developments, *Chem. Soc. Rev.*, 2017, **46**, 7548–7596.
56 Y. Qu, F. Li and M. Zhao, Efficient hydrogen isotopologues separation through a tunable potential barrier: The case of a C_2N membrane, *Sci. Rep.*, 2017, **7**, 1483.
57 M. Li, L. Wang, H. Lei, Y. Yang, Y.-Q. Li, M. Zhao, J. Guan, W. Li and Y. Qu, Efficient helium and helium isotopes separation by phosphorus carbide P_2C_3 membrane, *Adv. Theory Simul.*, 2022, **5**, 2100327.
58 M. I. Hernández, M. Bartolomei and J. Campos-Martínez, Transmission of helium isotopes through graphdiyne pores: Tunneling versus zero point energy effects, *J. Phys. Chem. A*, 2015, **119**, 10743–10749.
59 A. Cedillo, Quantum mechanical tunneling through barriers: A spreadsheet approach, *J. Chem. Educ.*, 2000, **77**, 528.
60 M. Bartolomei, E. Carmona-Novillo, M. I. Hernández, J. Campos-Martínez and R. Hernández-Lamoneda, Long-range interaction for dimers of atmospheric interest: dispersion, induction and electrostatic contributions for O_2–O_2, N_2–N_2 and O_2–N_2, *J. Comput. Chem.*, 2011, **32**, 279–290.
61 M. S. Motallebiour, J. Karimi-Sabet and A. Maghari, ^{4}He/^{3}He separation using oxygen-functionalized nanoporous graphene, *Phys. Chem. Chem. Phys.*, 2019, **21**, 12414–12422.
62 Z. Zhou, Permeance should be used to characterize the productivity of a polymeric gas separation membrane, *J. Membr. Sci.*, 2006, **281**, 754–756.
63 H. W. Kim, H. W. Yoon, S.-M. Yoon, B. M. Yoo, B. K. Ahn, Y. H. Cho, H. J. Shin, H. Yang, U. Paik, S. Kwon, J.-Y. Choi and H. B. Park, Selective gas transport through few-layered graphene and graphene oxide membranes, *Science*, 2013, **342**, 91–95.
64 C. Sun, M. S. H. Boutilier, H. Au, P. Poesio, B. Bai, R. Karnik and N. G. Hadjiconstantinou, Mechanisms of molecular permeation through nanoporous graphene membranes, *Langmuir*, 2014, **30**, 675–682.
65 **https://en.wikipedia.org/wiki/Spherical_harmonics#Real_form**.
66 J. T. Muckerman, Some useful discrete variable representations for problems in time-dependent and time-independent Quantum mechanics, *Chem. Phys. Lett.*, 1990, **173**, 200–205.
67 E. J. Heller, Time-dependent approach to semiclassical dynamics, *J. Chem. Phys.*, 1975, **62**, 1544–1555.
68 M. D. Feit, J. A. Fleck and A. Steiger, Solution of the Schrödinger equation by a spectral method, *J. Comput. Phys.*, 1982, **47**, 412–433.
69 D. Zhang and J. Z. H. Zhang, Full-dimensional time-Dependent treatment for diatom-diatom reactions: The H_2 + OH reaction, *J. Chem. Phys.*, 1991, **101**, 1146–1156.